UC Irvine
UC Irvine Previously Published Works

Title

Chapter 5 Refractory plasmonic materials

Permalink

Authors

Chang, Ching-Wen

Mishra, Ragini

Ahn, Hyeyoung

et al.

Publication Date

2024

DOI

Copyright Information

Peer reviewed

Refractory plasmonic materials

5

Ching-Wen Chang[1], Ragini Mishra[1], Hyeyoung Ahn[2], Ho Wai Howard Lee[3] and Shangjr Gwo[1]

[1]*Department of Physics, National Tsing Hua University, Hsinchu, Taiwan*
[2]*Department of Photonics, National Yang Ming Chiao Tung University, Hsinchu, Taiwan*
[3]*Department of Physics and Astronomy, University of California at Irvine, Irvine, CA, United States*

5.1 Introduction

Recently, refractory plasmonics [1−10] has attracted a lot of attention due to the importance of high-temperature, high-power energy applications, such as solar energy harvesting, photothermal energy conversion, photochemical reaction, and photocatalysis, which require operations under harsh environmental conditions. In comparison to conventional plasmonic materials [11−15], ideal refractory plasmonic materials possess the properties of low cost, low plasmonic loss, as well as thermal, mechanical, and chemical stabilities [1−10]. Additionally, suitable spectral range and integrability with semiconductor technology are also important considerations. Compared to the most popular plasmonic materials, conductive transition metal nitrides (TMNs, as shown in Fig. 5.1 and Table 5.1), including group IVB nitrides (titanium nitride [TiN], zirconium nitride [ZrN], hafnium nitride [HfN]) and group VB nitrides (vanadium nitride [VN], niobium nitride [NbN], tantalum nitride [TaN]), are promising plasmonic materials for refractory plasmonic applications due to their high electrical conductivities, extremely high melting temperature, and excellent mechanical, thermal, chemical properties [16−19]. The fundamental material properties of TMNs have been studied for several decades for various applications requiring mechanical hard and corrosion-resistant operational conditions [17,18,20−22]. Recently, excellent material properties of superconducting TMNs (TiN, NbN, and TaN) have also made them a widely applicable material platform for developing critical components in quantum information technologies [19], such as quantum computation [23] and quantum communication [24].

Most of the group IVB and VB TMNs discussed here can form crystals with the cubic rocksalt (NaCl) structure (B1 TMNs) [16,18,19], and they are often called "interstitial metal compounds" in which the nitrogen atoms are inserted into the interstitial sites of the parent face-center cubic (fcc) lattices of transition metals. As shown
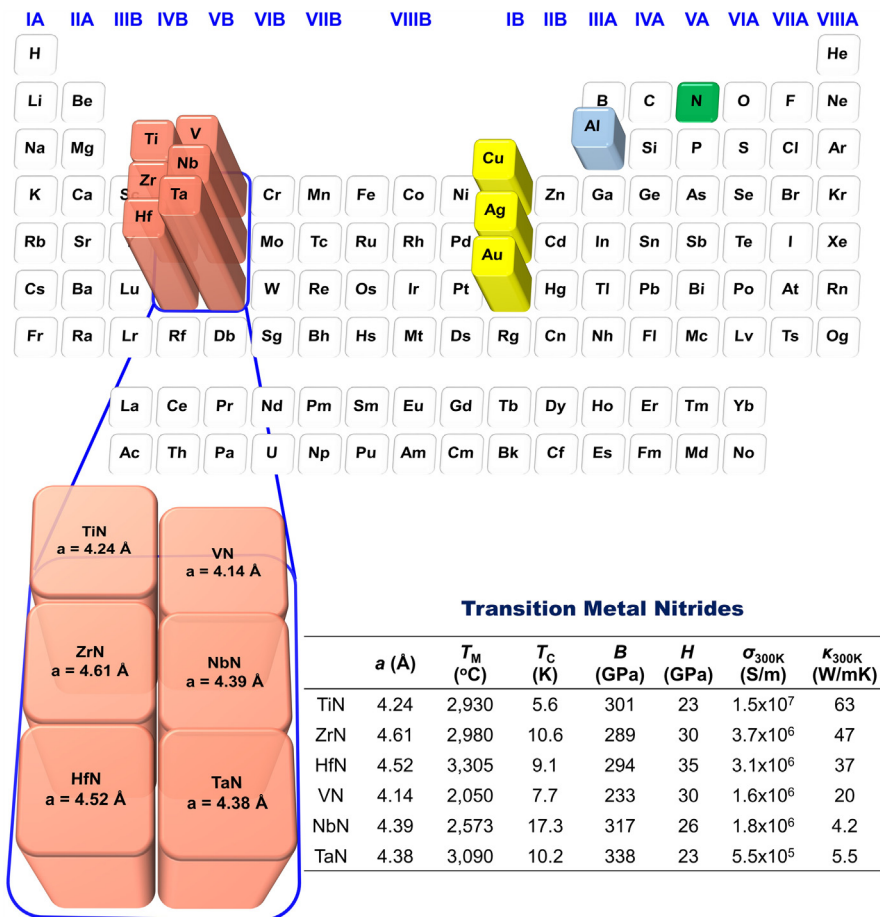
FIGURE 5.1 Periodic table of the elements.

An excerpt of the periodic table of the elements, which are the usual constituents of plasmonic materials and refractory transition metal nitrides. The lattice constant (a), melting temperature (T_M), superconducting critical temperature (T_C), bulk modulus (B), mechanical hardness (H), electrical conductivity at room temperature (σ_{300K}), and thermal conductivity at room temperature (κ_{300K}) are presented in a table, adapted from ref. [16].

Transition Metal Nitrides

	a (Å)	T_M (°C)	T_C (K)	B (GPa)	H (GPa)	σ_{300K} (S/m)	κ_{300K} (W/mK)
TiN	4.24	2,930	5.6	301	23	1.5×10^7	63
ZrN	4.61	2,980	10.6	289	30	3.7×10^6	47
HfN	4.52	3,305	9.1	294	35	3.1×10^6	37
VN	4.14	2,050	7.7	233	30	1.6×10^6	20
NbN	4.39	2,573	17.3	317	26	1.8×10^6	4.2
TaN	4.38	3,090	10.2	338	23	5.5×10^5	5.5

in Fig. 5.1, the high electrical (σ) and thermal (κ) conductivities, high melting temperature (T_M), and high mechanical hardness (H) result from an unusual combination of covalent compound, ionic crystal, and metal. The optical properties of group IVB nitrides (B1 TiN, ZrN, and HfN) are free-electron-like (Drude-like) due to negligible interband transitions, which make them attractive for optical applications [20]. Very recently, they have also been used as plasmonic materials for full-color applications

Table 5.1 Comparison of Au, Ag, Cu, Al, and TiN as plasmonic materials. The material costs are compiled from London Metal Exchange (LME) prices (January−October, 2022) and Asian Metal (AM) prices (January−October 2022).

Material	Au	Ag	Cu	Al	TiN
Price ($US/ounce)	1,650−2,000	18−28	0.23−0.33	0.063−0.119	Ti:0.21−0.58
Abundance in Earth's crust (mg/kg)	4×10^{-3}	7.5×10^{-2}	60	8.23×10^{4}	Ti:5.65×10^{3}
Melting point (°C)	1,064	961	1,085	660	2,930
Vickers hardness (GPa)	0.216	0.251	0.343−0.369	0.167	18−21
Interband transition (eV)	2.54	3.96	2.19	1.55	2.75
Plasmon energy (eV)	8.69	9.12	8.18	11.63	5.7−8.7
Spectral range	Green to IR	NUV to IR	Green to IR	DUV to IR	Blue to IR

[7,9,18,20,21] in the visible range. The as-grown B1 TiN, ZrN, and HfN films show gold-like yellow color (bright yellow for TiN (see Fig. 5.2A,B, [7,9]), and become gradually paler for ZrN and HfN [18]).

Among group IVB and VB TMNs, TiN has the highest electrical conductivity (see the comparison with other TMNs in Fig. 5.1), and it has attracted most of the attention as the refractory plasmonic materials (alternative to Au) owing to excellent optical properties in the visible and near-infrared regions, negligible interband absorption in the blue region (as shown in Fig. 5.2B), high melting temperature ($\sim$3000°C), extreme mechanical hardness, and stability against material degradation. In addition, TiN possesses complementary metal−oxide-semiconductor (CMOS) and biological compatibilities. As a result, TiN-based plasmonics is particularly suitable for optical devices [1−10,15,20,21,25−33], energy harvesting [7,9,10,29,34−38], biomedical applications [39,40], CMOS-integrated devices [41], and superconducting quantum devices [42−44]. Especially, TiN plasmonic metasurfaces have been demonstrated as optical broadband absorbers and narrowband emitters [7,9,34−38].

Traditionally, TiN is heavily used in semiconductor and superconducting devices, such as diffusion barriers, metallization contacts, and superconducting device structures, and, most of the TiN films reported in the literature were grown by reactive sputtering [2,3,5,8,15,20,21,25−31,43,45], chemical vapor deposition
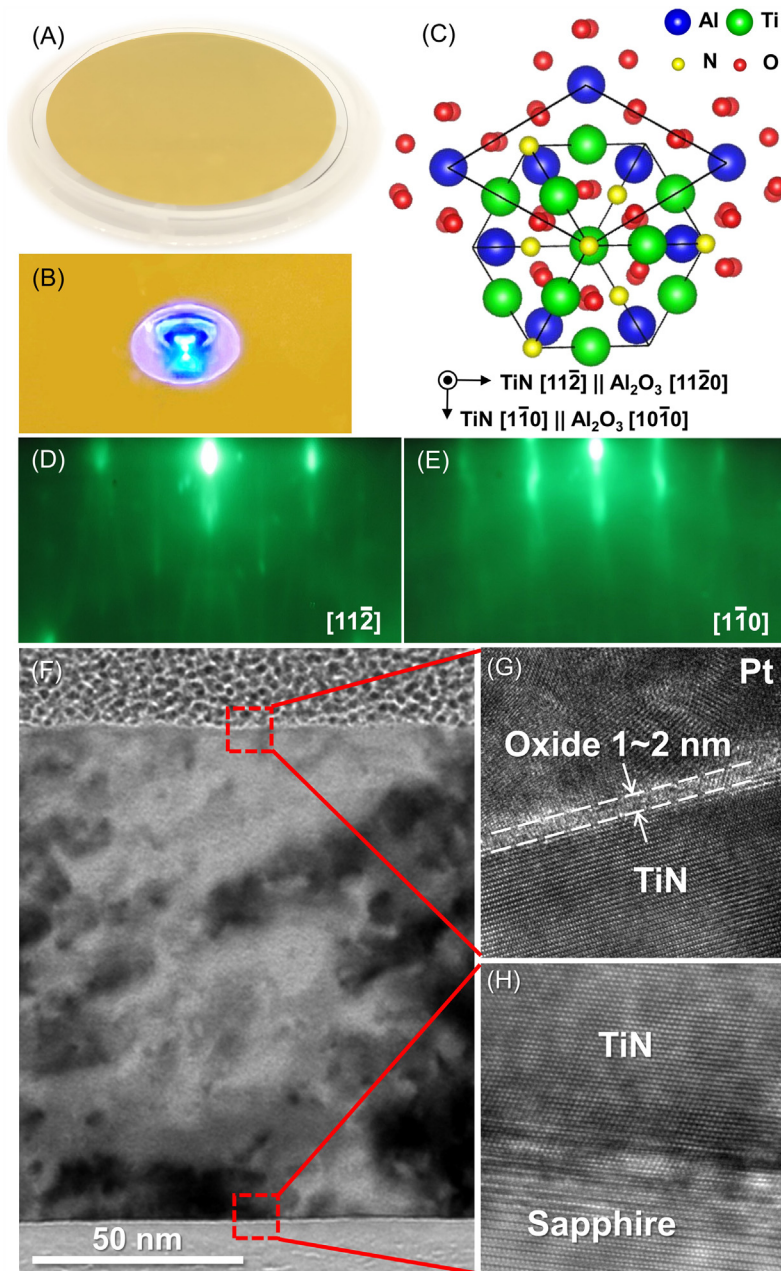
FIGURE 5.2

(A) Optical image of a TiN epitaxial film grown on a two-inch, c-plane sapphire wafer. (B) Optical image showing blue light transmission through the TiN epitaxial film grown by molecular-beam epitaxy (MBE) due to higher interband transition energy (2.75 eV), in comparison to Au (2.54 eV). (C) Schematic drawing of in-plane epitaxial relations of TiN film grown on c-sapphire. (D, E) Reflection high energy electron diffraction (RHEED) patterns obtained along the $[11\bar{2}]$ and $[1\bar{1}0]$ directions (15 kV electron beam at 1.5 A). (F) Transmission electron microscopy (TEM) image of a 120-nm-thick TiN epitaxial film grown on *c*-sapphire by MBE. (G) High-resolution TEM image revealing the native oxide layer on top of the MBE-grown TiN film. (H) High-resolution TEM image showing an abrupt film/substrate interface.

(CVD), atomic layer deposition (ALD) [44,46], and pulsed laser deposition (PLD) [47,48]. However, growth of high-quality stoichiometric TiN films requires an ultraclean growth environment because of the propensity of titanium to react with residue gases. It is well known that titanium is an active absorbing agent, which is widely used as a sublimation pump material in ultrahigh vacuum (UHV) systems. Therefore, the achievable material properties of conventional TiN films prepared by reactive sputtering or chemical vapors have a high propensity to form titanium oxynitride and other forms of nonstoichiometric (nitrogen-deficient compounds) titanium nitride films. Recently, several groups have reported the method of nitrogen (N_2)-plasma-assisted molecular-beam epitaxy (MBE) in a UHV environment for the growth of high-quality, stoichiometric TiN epitaxial films [7,9,10,49,50]. In this chapter, we will focus on the refractory plasmonic applications based on the MBE-grown TiN for both thin (<1000 nm) and ultrathin (<10 nm) films. Most of the examples shown here are adopted from our recently published results [7,9,10,51,52].

## 5.2 Epitaxial growth of rocksalt TiN(111) films on sapphire

In comparison to semiconductors and insulators, metals have high surface energies due to a large number of unsaturated dangling bonds. Therefore typical metals, such as Au, Ag, and Cu, do not properly wet on most of the commercially available substrates (Si, GaAs, Al_2O_3, SiO_2, TiO_2, etc.), resulting in polycrystalline thin film growth with large surface roughness and sometimes atomically diffused interfaces [16]. For the development of tunable ultrathin plasmonic devices [53,54], special growth techniques are necessary to prepare ultrathin metal films [55,56]. TMNs offer an opportunity for the epitaxial growth of metals (or superconductors) on semiconductors or oxide substrates due to their combination of covalent and metallic bonding.

As discussed above, most of the TMNs crystallize in the rocksalt structure with octahedral coordination and a high degree of iconicity in their chemical bonding. Therefore, substrate materials with commensurate crystal structures can be found. For example, the (111)-plane lattice parameters of the rocksalt crystal structure of TiN, NbN, and other TMNs are close to the c-plane lattice parameters of wurtzite SiC, AlN, and GaN, which have the required hexagonal symmetry for epitaxial growth. Indeed, these commensurate substrates have led to recent demonstrations of epitaxial heterostructures of NbN and TiN on SiC, AlN, and GaN substrates by MBE [10,57,58]. Similarly, the (111)-oriented TiN epitaxial films can also be grown on the c-plane (0001) sapphire substrates, as well as lattice-matched MgO(111) and MgO(001) substrates with a rocksalt lattice parameter $a =$ 4.21 Å. In comparison, sapphire wafers are available in high crystalline quality, large sizes, and low costs. Especially, sapphire substrates have been widely used for heteroepitaxy of group-III nitrides (AlN, GaN, and InN).

In our recent studies [7,9], (111)-oriented TiN thin films were epitaxially grown on *c*-plane (0001) sapphire substrates (Fig. 5.2A). The root-mean-square roughness is measured by AFM to be about <1 nm [51]. The in-situ reflection high energy electron diffraction (RHEED) patterns (Fig. 5.2D,E) confirm the epitaxial relationships (shown in Fig. 5.2C). Furthermore, the ex-situ transmission electron microscopy (TEM) images testify to the high crystalline quality of as-grown TiN films (Fig. 5.2F,G,H). The cross-section TEM images indicate the formation of an abrupt interface between the TiN film and the sapphire substrate, and the high-resolution TEM images of the TiN region show that the (111) layer spacing is about 2.4 Å, consistent with the X-ray diffraction (XRD) measurement results, indicating a close-packed rocksalt lattice structure, where nitrogen occupies octahedral interstitial sites in the Ti face-centered cubic lattice.

One of the major challenges for TiN-based plasmonic devices is oxygen contamination in the grown TiN films since the O and N exchange reaction is thermodynamically favorable. For most of the plasmonic applications demonstrated so far, TiN films are deposited by reactive sputtering, which is not performed under the preferred ultrahigh vacuum condition. Therefore, oxidation is a major issue [9,59,60], which could cause the degradation of the film's electrical and optical properties, such as electrical resistivity, optical response, and even thermal stability. Recently, we reported that epitaxial growth of the oxidation-resistant TiN(111) film on sapphire grown by nitrogen plasma-assisted MBE could provide an optimized approach for refractory plasmonics requiring excellent plasmonic properties, as well as high thermal and chemical stabilities [9]. Especially, a single-TiN-layer (~200-nm-thick) metasurface broadband absorber with ~90% absorptivity over the visible spectrum is demonstrated. Furthermore, we show that the metasurface absorber made from the MBE-grown TiN film could sustain vacuum annealing at 850°C and irradiation under 130 suns in the ambient environment without appreciable degradation in optical response and structural integrity. In comparison, the same absorber structure made from the sputtered TiN film shows inferior optical performance, as well as degraded thermal and chemical stabilities due to a significant amount of oxygen contamination in the film.

The oxygen-free, stoichiometric nature of the MBE TiN film can be confirmed by X-ray photoelectron spectroscopy (XPS) measurements [9,59]. The surface of as-grown TiN film after exposure to the atmosphere contains a thin titanium oxide surface layer, and the layer thickness is self-limited (i.e., saturated at constant temperature and oxygen partial pressure), as shown in Fig. 5.2H. This is similar to the surface oxidation case of aluminum film, which can act as a native passivation layer. Fig. 5.3A,B shows the Ti $2p$ XPS spectra at the top film surfaces, which consist of pairs of Ti $2p_{3/2}$ and Ti $2p_{1/2}$ spin-orbit split peaks, where the higher-binding-energy pair can be attributed to the Ti−O bonding and the peak energies correspond close to the TiO_2 phase with a layer thickness less than the photoelectron escape depth (about a few nanometers). As confirmed by high-resolution TEM (Fig. 5.2H), the self-limited native titanium oxide layer of MBE-grown TiN film is indeed about 1−2 nm in thickness.
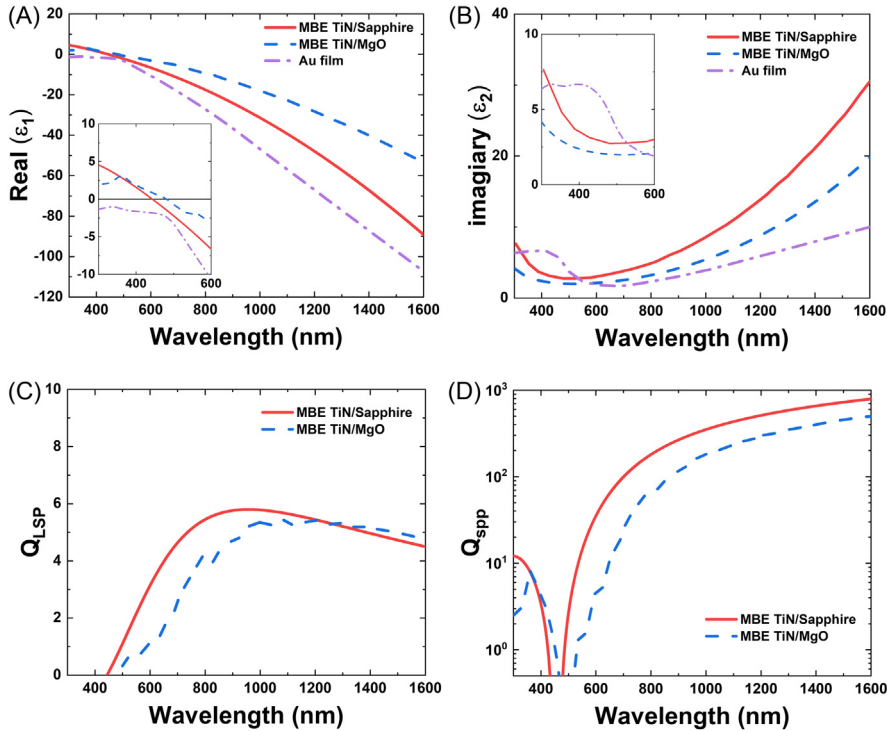
FIGURE 5.3

(A, B) Dielectric functions measured by spectroscopic ellipsometry (SE) for an MBE-grown TiN/sapphire film (from our group), and an MBE-grown TiN/MgO film (reported by Maurya et al. [49]), and an Au(111) film grown on mica. According to the SE data for the TiN/sapphire film, the characteristic surface plasmon energy is 2.6 eV ($\lambda_{sp} = 470$ nm, $\varepsilon_1 = -1$) at the TiN/air interface and the epsilon-near-zero (ENZ) point is about 2.8 eV. Comparison of quality factors for (C) localized surface plasmon (LSP), $Q_{LSP} = (\omega(d\varepsilon_1/d\omega)/2\varepsilon_2)$ and (D) surface plasmon polariton (SPP), $Q_{SPP} = 2(\varepsilon_1 + \varepsilon_d)(\varepsilon_1)^2/(\varepsilon_1\varepsilon_d\varepsilon_2)$, for the cases of MBE-grown TiN films on sapphire and MgO substrate, respectively.

On the other hand, Fig. 5.3C,D shows the pristine Ti $2p$ XPS spectra in the bulk of MBE and TiN film after Ar-ion milling, which consist of pairs of Ti $2p_{3/2}$ and Ti $2p_{1/2}$ spin-orbit split peaks (Ti−N bonding) with electron binding energies of 455.0 eV and 461.0 eV for both as-grown TiN films (Fig. 5.3C) and Ar-ion-milled films (Fig. 5.3D). The measured Ti $2p$ peak energies are in good agreement with that reported for single-crystalline oxygen-free TiN measured by XPS [61]. It should be noted that the broad (FWHM ~ 4 nm) shape-up peaks of TiN bonding (shoulder peaks near the Ti $2p_{3/2}$ and Ti $2p_{1/2}$ spin-orbit split peaks at higher binding energies) are spectrally overlapped with the Ti $2p$ peaks of O−Ti−N bonding.

The nitrogen N 1s XPS peaks have also been investigated (shown in Fig. 5.2E,F) and their binding energies are only slightly different: 397.1 eV (MBE TiN) versus 397.2 eV (sputtered TiN). From the Ti 2p and N 1s XPS results, it is clear that the amount of oxygen in the sputtered TiN film cannot be directly identified by Ti 2p and N 1s XPS measurements without proper surface preparation. After Ar-ion milling, the O 1s XPS spectra in the bulk of the TiN films (shown in Fig. 5.3G,H) can precisely determine the absence of MBE TiN, and the presence of sputtered TiN with oxygen content. For revealing the detailed chemical information in the bulk of the TiN films, continuous Ar-ion milling was performed for the elemental depth profiles of Ti, O, and N across the film by recording corresponding XPS peak intensities versus the milling time. The concentration depth profiles of Ti, O, N, and Al from the top of the film to the interface with the sapphire substrate, as shown in Fig. 5.3I,J. It can be clearly seen that the atomic concentrations of Ti and N in MBE TiN are close to 1:1, while the element composition of the sputtered TiN film corresponds to the TiO_xN_{1-x} ($x \approx 0.1-0.2$) alloy.

5.3 Optical properties of thick TiN(111) films grown on sapphire

The dielectric properties of the metal can be expressed by the dielectric function of frequency, $\varepsilon(\omega) = \varepsilon_1(\omega) + i\varepsilon_2(\omega)$. Fig. 5.4A,B show the dielectric functions of MBE-grown TiN films with respect to an Au film, which were measured by spectroscopic ellipsometry (SE) and fitted by using the Drude-Lorentz model [7]. In this model, the Drude term represents the contribution from the conduction electrons, and the Lorentz term stands for the interband transitions. In the stoichiometric case, the color of the as-grown TiN film (120 nm in thickness) looks very much like gold (Fig. 5.2A). The film reflectivity at normal incidence, estimated by using the optical dielectric function, is as high as $\sim 90\%$ at normal incidence when the wavelength is close to the yellow. This is why the TiN film exhibits a mirror-like surface, as shown in Fig. 5.2A.

In metal thin-film optics, the imaginary part of permittivity (ε_2) is related to the optical losses, such that low-loss plasmonic materials have small ε_2 values. In the visible range (400−700 nm), ε_2 measured for the MBE-grown TiN is close to the case of Au film and much smaller than the case of sputtered TiN films [7]. For the blue region of the visible, the ε_2 of Au is larger than TiN because of a strong interband transition in Au (see Table 5.1). For noble metals such as Au, Ag, and Cr, interband transitions exhibit a step-like threshold behavior. When the incident photon energy is higher than ~ 2.54 eV (i.e., wavelength shorter than 500 nm), electron-hole pairs are predominantly excited in gold instead of surface plasmons. This threshold behavior means that surface plasmon phenomena can be observed only for incident photon energies lower than the interband transition
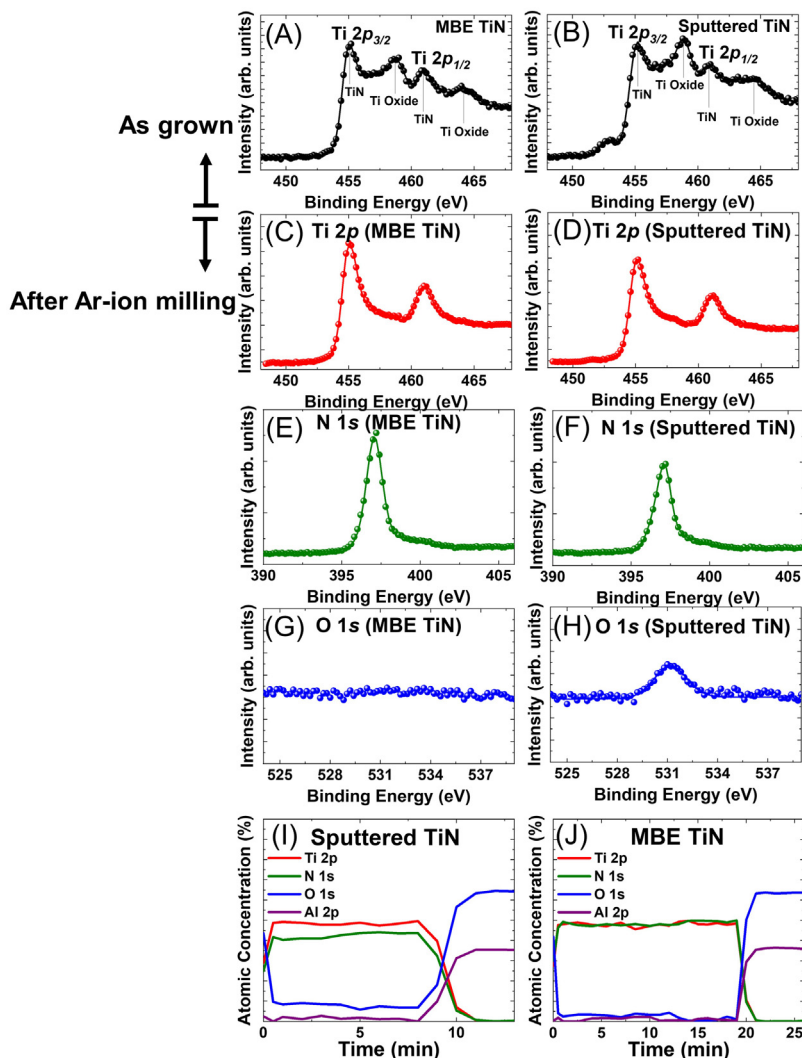
FIGURE 5.4 XPS analysis of MBE and sputtered TiN films.

(A, B) Ti 2p core-level spectra from the MBE-grown and sputtered TiN films before Ar-ion milling show the presence of a TiO$_x$ surface layer. (C, D) Ti 2p core-level spectra from the MBE-grown and sputtered TiN films after Ar-ion milling show only the TiN-related 2p doublet lines (2$p_{3/2}$, 2$p_{1/2}$) with binding energies 455.0 eV and 461.0 eV. The shakeup peaks at higher binding energies are also visible. (E, F) N 1s core-level spectra show the N 1s binding energies are 397.1 eV and 397.2 eV for the MBE-grown and sputtered TiN films, respectively. (G, H) N 1s core-level spectra confirm the absence and presence of oxygen after Ar-ion milling inside the MBE and sputtered TiN films, respectively. (I, J) Atomic concentration depth profiles with respect to the Ar milling time from top to bottom. The MBE-grown TiN profile shows that the Ti and N concentration is close to 1:1, in contrast to the case of the sputtered TiN film, which has a significant amount of oxygen contamination (i.e., the sputtered film is actually TiO$_x$N$_{1-x}$).

All figures are reproduced with permission [9]. Copyright 2021 American Chemical Society.

energy. Besides ε_2, ε_1 also plays an important role since plasmonic materials allow for stronger field confinement when the ε_1 value is larger. For this reason, we express the figures of merit in terms of both ε_1 and ε_2, as shown in Fig. 5.4C,D.

Based on the measured dielectric function, the screening plasmon frequency (i.e., the epsilon-near-zero (ENZ) point, $\varepsilon_1(\omega_{ENZ}) = 0$, as shown in the inset of Fig. 5.4A) can be experimentally determined to be $\hbar\omega_{ENZ} = 2.8$ eV (λ_{ENZ} ~ 443 nm), which is significantly larger than the value reported by the previous experimental studies (note that when the real part of dielectric function is greater than zero, it is no longer a plasmonic material). In general, nonstoichiometric and ultrathin TiN films exhibit redshifts of λ_{ENZ}. Our optical measurement results indicate that the MBE-grown TiN films show excellent plasmonic properties. Therefore, not only can we replace TiN for Au in the visible and near-infrared spectral regions, but also TiN outperforms Au in the blue region. Furthermore, ultrathin TiN films can be used as a plasmonic material for both tunable properties [62−64] and ENZ applications [65−67], which require a small ε_2 value when $\varepsilon_1 \approx 0$.

5.4 Ultrathin TiN epitaxial films grown on sapphire: tunable electrical and optical properties

The optical and electrical properties of metallic and metal−oxide films can be manipulated by varying the film thickness [53,54,62−64], and the large enhancement of nonlinear coefficients has also been reported for ultrathin films [65]. As the film thickness decreases, the metallic reflectance is largely decreased, and the transmittance is increased up to $\geq 75\%$ for ≤ 5 nm TiN films [51]. Ultrathin TiN films also possess high electrical conductivity, so combined with high optical transmittance, it opens potential applications as thermally stable, transparent, and conductive electrodes. Moreover, the electrical conductivity of ultrathin TiN film is critically dependent on film quality and defects, including oxygen content and noncontinuous film morphology.

When the film thickness is reduced to less than a critical value known as percolation thickness, it is very difficult to deposit ultrathin and continuous noble metal films with smooth surface morphology [68]. For example, the percolation thickness for gold is in the range of 6−10 nm, limiting the device's dimension. In the case of TiN film, single-crystalline, stoichiometric TiN films have recently been grown by the MBE method under the UHV environment [7], but the growth of ultrathin films with high crystalline quality is still a challenge. To clarify this issue, we have recently prepared ultrathin TiN epilayers with 2−10 nm thickness via MBE growth. Owing to the UHV growth conditions, the influence of oxygen content on ultrathin films of <4 nm is greatly reduced. Fig. 5.5A shows the X-ray diffraction (X-ray wavelength of 1.54 Å) curves of TiN with different thicknesses. A peak centered at 36.8° corresponds to TiN (111), while another
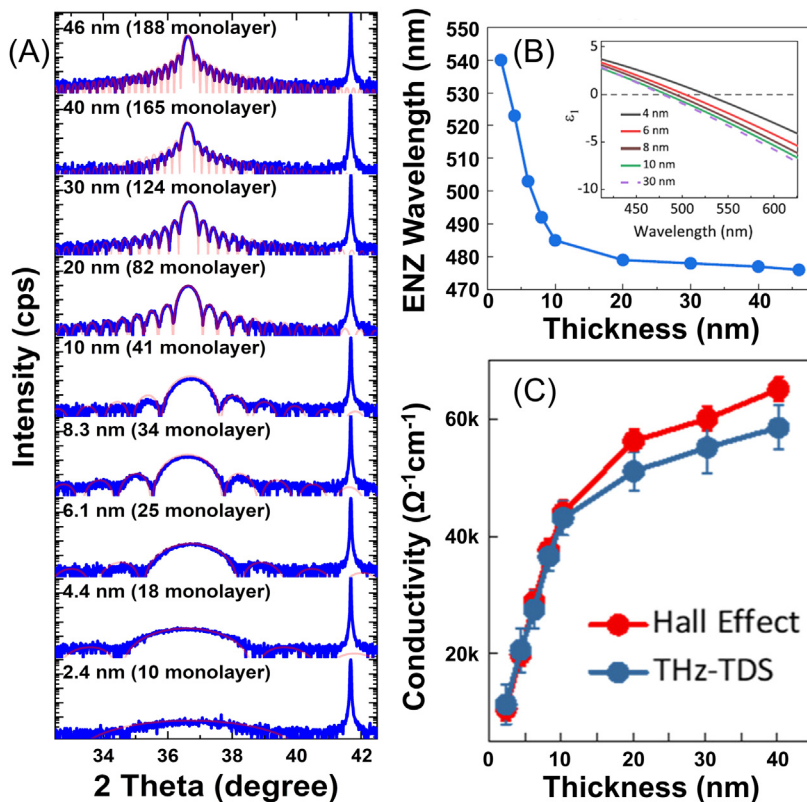
FIGURE 5.5

(A) The 2-theta scans of X-ray diffraction (XRD) are conducted on a series of ultrathin TiN (111) films with different thicknesses. The numbers of atomic monolayers are determined by satellite fringes of XRD. The red lines are fitted well to the experimental data (blue line). (B) Plot of ENZ wavelength (λ_{ENZ}) as a function of film thickness. Inset: ε_1 near the interband edge for films with different film thicknesses. (C) Comparison of DC conductivity measured by Hall effect measurements and THz-TDS.

Reproduced with permission [51]. Copyright 2022 American Chemical Society.

one at 41.7° originated from a *c*-plane sapphire substrate. Despite the broadening of peak width due to decreasing thickness for thinner films (size effects), clear XRD peaks from <5 nm films confirm the high crystalline quality of MBE-grown TiN ultrathin films.

The optical properties, in particular the dielectric properties of ultrathin TiN films, are explored by using SE. The Drude-Lorentz model was applied to fit the SE data from ultraviolet to near-infrared region. Fig. 5.5B shows the thickness dependence of ENZ wavelength of ultrathin TiN films, which is determined from the zero-crossing dielectric function ε_1 as shown in the inset. The ENZ

wavelength of thick films (>20 nm) is ~ 475 nm and continuously redshifts to 530 nm with the reduction in film thickness, enabling the tunability of plasmonic frequency. Notably, there is no large deviation in ENZ wavelength for films with a thickness of less than 4 nm, which is often observed for sputtered thin TiN films. This confirms that ultrathin films grown under the UHV environment achieve high quality without oxygen-related defects.

As the thickness is reduced, the carrier density is reduced and influences the electrical conductivity. In order to realize the electrical properties of ultrathin TiN films, two independent methods, terahertz time-domain spectroscopy (THz-TDS) and Hall measurements, were employed for investigation. The former is an optical and noncontact method, and the latter is a contact method. Fig. 5.5C shows the film thickness dependence of direct current (DC) conductivity (σ_{DC}). Thick TiN films are highly conductive with $\sigma_{DC} \sim 6.5 \times 10^4 \, \Omega^{-1}\text{cm}^{-1}$ and gradually reduced to $\sim 1.1 \times 10^4 \, \Omega^{-1}\text{cm}^{-1}$ for the 2.4-nm-thick film. Here, one thing to note is that σ_{DC} measured by the Hall method is in good agreement with that determined by THz-TDS. It is in sharp contrast to previous reports that there is a large deviation between optically and electrically measured electrical conductivities caused by morphological nonuniformity in ultrathin (<4 nm) films grown under atmospheric environments [69].

These results reveal that MBE-grown ultrathin TiN films with thickness >3 nm are morphologically smooth and have high crystallinity, as well as high optical transparency and electrical conductivity for refractory ultrathin TiN applications, allowing for the development of CMOS-compatible electrode materials to replace conventional metal oxide electrodes.

5.5 Refractory plasmonics for solar energy harvesting and optical sensing

In solar cell applications, the Shockley-Queisser (SQ) limit is a theoretical upper bound of solar energy conversion efficiency using a single semiconductor p-n junction, which is $\sim 41\%$ for maximum sunlight concentration and $\sim 31\%$ without concentration [70]. The SQ limitation originates from the broadband nature of the solar spectrum and the semiconductor bandgap: While photons are not absorbed if the incident photon energy is less than the semiconductor bandgap, photons with energy greater than the bandgap are absorbed with some energy loss due to fast electron-hole pair relaxation to the band edges.

To overcome this limitation (broad solar spectrum), the concept of a solar thermophotovaltic (STPV) system has been proposed and demonstrated by including an intermediate light absorption (broadband)/emission (narrowband) element between the sunlight and the solar cell [71–75]. In essence, this intermediate element acts as an alternative "Sun" for solar cells [73], which can absorb the entire solar spectrum and be heated to emit a narrowband spectrum tailored to match

the desired semiconductor photovoltaic element. The utmost advantage of STPV is that virtually all solar energy is converted into electrical energy, and an ideal intermediate element can tremendously boost the overall conversion efficiency. Based on a simple thermodynamic model and assuming a Sun temperature of 6000 K and an ambient temperature of 300 K, the ideal STPV system could attain a maximum efficiency of 85%, which occurs when the intermediate blackbody is at the optimal temperature of $T = 2544$ K [75−77].

In practice, it is difficult to operate at this temperature, and an ideal conversion efficiency as high as 70% could be achieved at a moderate temperature of 1000 K, which is already much better than the SQ limit [77]. The progress of the SPTV system has, however, been slow due to the lack of reliable and sustainable optical materials, which can operate at these high temperatures. The best result reported to date is 3.2% (light-to-electricity efficiency) using a broadband absorber ("dark" absorber) made of vertically aligned multiple-walled carbon nanotubes, which is heated to ∼1300 K [78]. Furthermore, due to the propensity of material degradation at high temperatures, a vacuum or inertia-gas-sealed environment is necessary for SPTV devices.

Recent advances in plasmonics and low-loss refractory plasmonic materials have provided new perspectives for SPTV developments. Especially it has been experimentally demonstrated that TiN is an excellent refractory plasmonic material for building optical broadband absorption and narrowband emitters [34−38]. In particular, TiN has been considered as the best candidate material for applications in photothermal energy conversion over a broad spectral region of the solar spectrum. According to a recent theoretical study [4], nanostructured TiN is an excellent broadband sunlight absorber due to strong plasmonic resonance ranging from 300 to 1300 nm, corresponding to the major sunlight spectral composition.

Recently, we have demonstrated that a single-layer metasurface broadband absorber made from the oxidation-resistant TiN(111) epitaxial film grown on c-plane sapphire by nitrogen-plasma-assisted MBE with ∼90% absorptivity over the visible spectrum [9]. This is accomplished by optimized plasmonic characteristics of the oxygen-free stoichiometric TiN film grown by MBE (see Fig. 5.6), in comparison with titanium oxynitride (TiO_xN_y) films prepared by the conventional reactive sputtering technique. In addition, the superb thermal and chemical stabilities of MBE-grown TiN metasurface are confirmed by irradiation under 130 suns in the ambient environment and vacuum annealing at 850°C (Fig. 5.6E,F).

Another important plasmonic application for optical sensing and solar energy harvesting applications is plasmon-mediated hot carrier injection, originally proposed by using the metal-semiconductor Schottky diode structure [79−83]. The low conversion efficiency and limited spectral range are, however, the major concerns. Compared to conventional silicon-based narrow bandgap (1.1 eV) Schottky diodes, hot-hole injection based on wide bandgap (3.4 eV) p-type gallium nitride (p-GaN) has been proposed to be an excellent semiconductor material for the broadband conversion of photonic energy, but the achievable efficiency is still rather low [84,85].
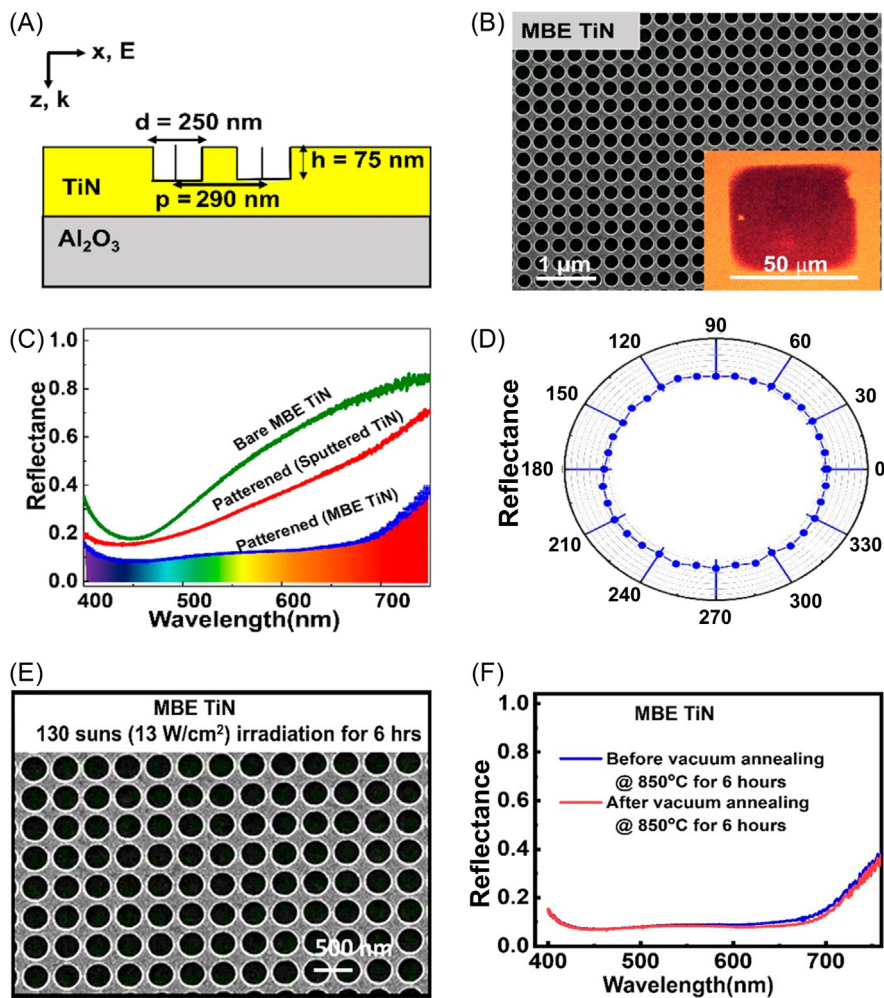
FIGURE 5.6

(A) Schematic drawing of the solar absorber consisting of a TiN nanohole array with optimized structural parameters: pitch (p) = 290, diameter (d) = 250 nm, and height (h) = 75 nm. The MBE-grown TiN epitaxial film was grown on a sapphire wafer with a film thickness of 200 nm. (B) Scanning electron microscopy (SEM) image of the TiN nanohole array and the inset shows an optical microscope image of the nanohole array, demonstrating a strong absorption in the full visible range. (C) Comparison spectra of optical absorbance measured for the MBE TiN metasurface (blue), the sputtered TiN metasurface (red) using the same nanoholes array structure, and a bare MBE-grown TiN film (green). (D) Polarized reflectance plot measured for the MBE TiN metasurface confirms that the broadband optical absorption is insensitive to the incident light polarization. (E) SEM image of the MBE TiN absorber under sun irradiation at an intensity of 130 suns (13 W/cm^2) for 6 h, and (F) Measured absorption spectra of the MBE TiN absorber before and after vacuum annealing at 850°C for 6 h for thermal stability testing.

Recently, we have demonstrated an efficient hot-hole injection mechanism based on the photoconductive TiN/p-type GaN (p-GaN) metal-semiconductor heterostructure grown by MBE [10]. Compared with the same heterojunction device structure using an MBE-grown TiN/n-GaN heterojunction, which exhibits a typical Schottky diode behavior, the photocurrent conversion efficiency can be increased four orders of magnitude (see device structure shown in Fig. 5.7A−C). Furthermore, an internal photovoltage, generated by interfacial charge transfer/separation across the TiN/p-GaN Schottky barrier (1.2 eV, see Fig. 5.7D), enables a self-sustainable photocurrent without external biasing (Fig. 5.7E,F). The refractory material properties (TiN, GaN, and sapphire substrate) and broadband conversion (1.2−3.4 eV or 365−1033 nm, which cover ~95% of the full solar energy spectrum) make this system capable of harvesting highly concentrated solar light at high temperatures.

It is worth noting that the MBE-grown TiN films have a rocksalt crystal structure with a titanium-terminated TiN(111) surface (the growth direction is along the [111] orientation). Therefore the TiN/GaN heteroepitaxial interface is formed between the nitrogen-terminated TiN(111) and the Ga-terminated GaN(0001) planes, as shown in Fig. 5.7A. This specific crystal polarity has an important consequence in the interface electronic structure since the TiN electronic structure is known to be polarity dependent, which leads to the photoconductive interface mode reported here at the TiN/p-GaN interface.

The XRD and TEM measurements confirm that the interface between TiN and GaN is extremely uniform. The atomically abrupt interface of the metal (TiN)/semiconductor (GaN) system is unveiled through high-resolution TEM images shown in Fig. 5.7A, which show that the interface possesses a low tensile strain (−5.14%). The high-resolution TEM image shows the line-cut along the [11$\overline{2}$] direction of the TiN lattice has a 2.58 Å lattice spacing. Judging by bulk lattice constants: 4.24 Å (TiN) along [001], 2.44 Å (TiN) along [11$\overline{2}$], and 3.19 Å (GaN) along the [0001] direction, 2.72 Å (GaN) along the [10$\overline{1}$0] direction, the tensile strain in the TiN epitaxial film relaxes through a 20 (TiN)/19 (GaN) coincident lattice match at the interface. The resulting tensile strain ($\Delta a/a_{sub}$) can be reduced to −5.14%. This result is very similar to the case reported earlier for the epitaxial growth of TiN(111) on the AlN(0001) surface [86].

5.6 Epsilon-near-zero application using ultrathin TiN epilayer

Two-dimensional semiconductors such as MoS_2 are considered as stable light emitters in contrast to quantum dots or dye molecules. However, strong emission is available only for monolayer MoS_2 with direct bandgap, and the monolayer has low absorption due to its angstrom scale thickness and low quantum efficiencies. Meanwhile, ENZ materials can be used to enhance the excitation fields in the
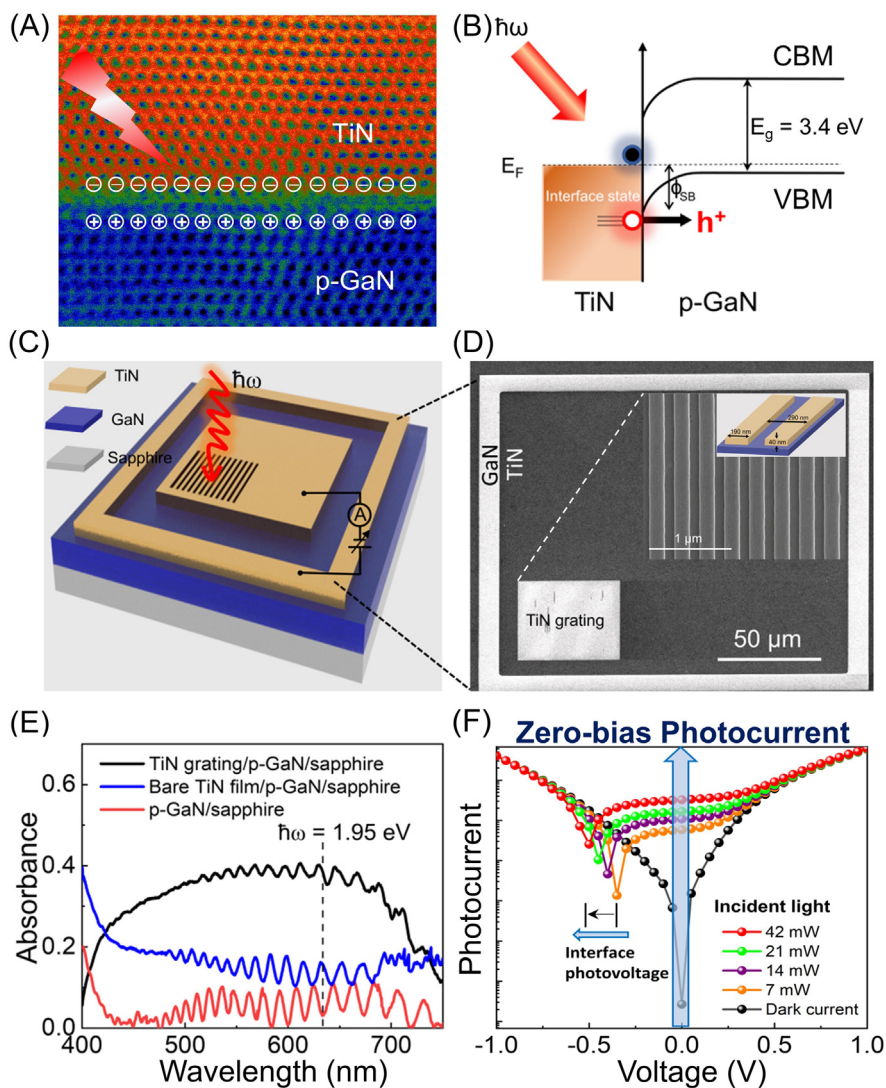
FIGURE 5.7

(A) High-resolution TEM image of TiN/GaN interface projected along the [1$\bar{1}$0] zone axis.
(B) Schematic band diagram of TiN/p-GaN Schottky junctions using the experimentally
determined valence-band (VB) and conduction-band (CB) barrier heights: 1.2 eV and
0.6 eV. (C) Schematic drawing of the TiN/p-GaN device. (D) SEM image of as-fabricated
TiN/p-GaN device. Inset is an SEM image of the nanoribbon grating structure patterned on
TiN/p-GaN by electron beam lithography (E) Optical absorption spectra of TiN grating
structure on p-GaN/sapphire, bare TiN film/p-GaN/sapphire, and p-GaN/sapphire
substrate, showing the grating is designed to have the maximum absorbance at 1.95 eV,
corresponding the energy of the transverse magnetic (TM)-polarized laser excitation light
(635 nm). (F) Semilog $I - V$ characteristics of the TiN/p-GaN device at different incident
optical intensities, showing the photoconductive behavior at zero bias voltage and varying
onset voltage shifts (from 0.35 to 0.50 V).

emitting layer and then combined with two-dimensional emitters, absorption and photoluminescence (PL) can be significantly enhanced by using interference effects in 2D materials backed with planar and nanostructured metallic reflectors [1−4], plasmonic resonances coupled to both excitation and emission fields [5,6]. Thin homogeneous TiN films with ENZ wavelengths in the visible spectrum are employed to realize this emission enhancement from a 2D emitter.

Fig. 5.8A depicts the schematic of the enhanced spontaneous emission from the MoS_2 monolayer on TiN ENZ substrate. The PL from MoS_2 flakes on thin ($\sim$50 nm) and thick ($\sim$130 nm) TiN films was measured using a confocal laser scanning fluorescence microscope with several excitation wavelengths across the ENZ wavelength. For comparison purposes, the assembly of emitter and substrate layers is prepared, which consists of a sapphire substrate, epitaxial or sputtered TiN films, an atomic layer deposited Al_2O_3 spacer layer, and MoS_2 monolayer flakes. The reference sample consists of MoS_2 flakes on a sapphire substrate. Fig. 5.8B exhibits the PL enhancement on TiN with respect to sapphire, in which emission of the MoS_2 on TiN (thickness 133 nm) is clearly much brighter than on sapphire. In addition, the PL enhancement depends on the excitation laser wavelength, as shown in Fig. 5.8B for four excitation wavelengths across the ENZ wavelength.

To gain insight into the dependence of the PL enhancement on excitation laser wavelength, we performed numerical calculations of fluorescence enhancement for an emitter embedded inside a multilayer geometry [7,8]. The total electromagnetic enhancement of the PL is the product of two contributions: excitation and emission enhancement. The excitation field enhancement due to the 133 nm thick MBE-grown TiN substrate varies with excitation wavelength. In order to experimentally verify this, we investigated the PL enhancement from MoS_2 − spacer − TiN stacks as a function of excitation wavelength for MBE-grown epitaxial TiN (58 nm and 133 nm) and sputtered TiN (51 nm and 146 nm). As a comparison, the result from the MoS_2 − spacer − Au stack (Au film thickness 100 nm) is also included. The experimental and calculated PL enhancements as a function of excitation wavelength are plotted in Fig. 5.8C. For the MBE-grown epitaxial TiN (black curves) having lower optical losses, the PL enhancement reaches about twofold enhancement as the transition from dielectric to metallic across the ENZ wavelength occurs. In contrast, the sputtered TiN samples (blue curves), having mismatched ENZ wavelength to the excitation wavelength, are all dielectric and thus do not exhibit the same trend as the MBE samples. The 133 nm-thick MBE TiN film has higher enhancement than the 58 nm-thick sample due to higher reflectivity, although the 58 nm sample has a smaller loss. It can be observed that epitaxial TiN and Au have comparable performance, especially above the ENZ wavelength of TiN, where its negative real permittivity becomes larger and more metallic.

In contrast, for thin spacers (<10 nm), PL enhancement peaks are observed near the ENZ wavelengths for both samples due to the enhanced absorption inside the MoS_2 layer at the ENZ wavelength of the TiN film (Fig. 5.8D). We expect the emission enhancement and manipulation of TiN to find widespread applications. In particular, the ultrathin TiN epitaxial films can switch from a poor
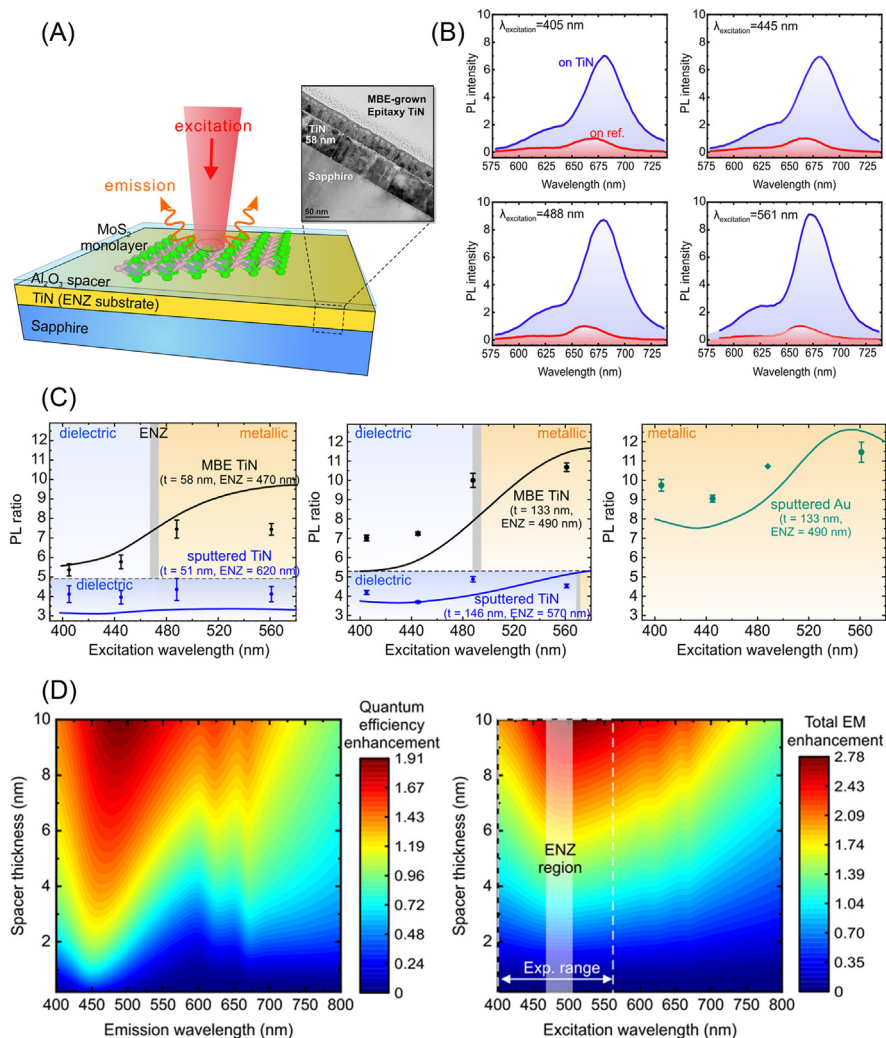
FIGURE 5.8

(A) Schematic drawing of enhanced spontaneous emission from a MoS_2 monolayer on TiN ENZ substrate. 30-nm Al_2O_3 spacer is deposited on TiN film to reduce the optical loss. Inset depicts a TEM image of the MBE-grown 58 nm TiN film on a sapphire substrate. (B) Photoluminescence (PL) spectra of MoS_2 monolayer on TiN excited with different excitation lasers at various wavelengths. Blue (red) curves are from MoS_2 on TiN (reference) substrate, respectively. (C) Measured and calculated PL enhancement of MoS_2 on TiN and Au films with 30 nm thick Al_2O_3 spacer with respect to that on the sapphire substrate. Black curves are from MBE-grown 58 nm and 133 nm TiN and blue curves are from sputtered 51 nm and 146 nm TiN, respectively. Gray vertical lines indicate the ENZ wavelengths of TiN films. (D) Quantum efficiency enhancement (left panel) and total electromagnetic enhancement (right panel) of in-plane dipoles in MoS_2 monolayer on titanium nitride (thickness 58 nm) for thin spacers (<10 nm).

(dielectric) to a good (metallic) reflector with applied voltage at a fixed wavelength in the visible range due to the electrically tunable permittivity of the films. This property may be of great importance to various optical, optoelectrical, display, and energy harvesting technologies.

5.7 Summary

Group IVB transition metal nitrides (TiN, ZrN, and HfN) are promising plasmonic materials for refractory plasmonic applications due to their high electrical conductivities, extremely high melting temperature, and excellent physicochemical properties, such as mechanical (ultrahardness), and chemical (corrosion resistance) stabilities. The use of TiN as a plasmonic metal offers other important advantages, such as the highest electrical conductivity among TMNs, broadband optical absorption from visible to infrared, tunable ENZ wavelengths of TiN ultrathin layers in the visible range, long carrier mean free path, and photon-induced charge separation at the metal-semiconductor interface. In particular, high-quality heteroepitaxy of TiN on sapphire and GaN substrates is now feasible. The refractory material properties of TiN, GaN, and sapphire allow for high-temperature operations under concentrated sunlight.

References

[1] U. Guler, A. Boltasseva, V.M. Shalaev, Refractory plasmonics, Science 344 (2014) 263−264.

[2] W. Li, U. Guler, N. Kinsey, G.V. Naik, A. Boltasseva, J. Guan, et al., Refractory plasmonics with titanium nitride: Broadband metamaterial absorber, Adv. Mater. 26 (2014) 7959−7965.

[3] P. Patsalas, N. Kalfagiannis, S. Kassavetis, Optical properties and plasmonic performance of titanium nitride, Materials 8 (2015) 3128−3154.

[4] M. Kumar, N. Umezawa, S. Ishii, T. Nagao, Examining the performance of refractory conductive ceramics as plasmonic materials: A theoretical approach, ACS Photonics 3 (2016) 43−50.

[5] L. Gui, S. Bagheri, N. Strohfeldt, M. Hentschel, C.M. Zgrabik, B. Metzger, et al., Nonlinear refractory plasmonics with titanium nitride nanoantennas, Nano Lett. 16 (2016) 5708−5713.

[6] A. Catellani, A. Calzolari, Plasmonic properties of refractory titanium nitride, Phys. Rev. B 95 (2017) 115145.

[7] W.-P. Guo, R. Mishra, C.-W. Cheng, B.-H. Wu, L.-J. Chen, M.-T. Lin, et al., Titanium nitride epitaxial films as a plasmonic material platform: Alternative to gold, ACS Photonics 6 (2019) 1848−1854.

[8] M.N. Gadalla, A.S. Greenspon, M. Tamagnone, F. Capasso, E.L. Hu, Excitation of strong localized surface plasmon resonances in highly metallic titanium nitride nanoantennas for stable performance at elevated temperatures, ACS Appl. Nano Mater. 2 (2019) 3444−3452.

[9] R. Mishra, C.-W. Chang, A. Dubey, Z.-Y. Chiao, T.-J. Yen, H.W. Howard Lee, et al., Optimized titanium nitride epitaxial film for refractory plasmonics and solar energy harvesting, J. Phys. Chem. C. 125 (2021) 13658−13665.

[10] R. Mishra, A. Dubey, C.-W. Chang, A. Ranjan, M.-Y. Lu, T.-J. Yen, et al., Epitaxial TiN/GaN heterostructure for efficient photonic energy harvesting, ACS Photonics 9 (2022) 1895−1901.

[11] W.A. Murray, W.L. Barnes, Plasmonic materials, Adv. Mater. 19 (2007) 3771−3782.

[12] M.B. Cortie, M.D. Arnold, V.J. Keast, The quest for zero loss: Unconventional materials for plasmonics, Adv. Mater. 32 (2020) 1904532.

[13] P.R. West, S. Ishii, G.V. Naik, N.K. Emani, V.M. Shalaev, A. Boltasseva, Searching for better plasmonic materials, Laser Photonics Rev. 4 (2010) 795−808.

[14] A. Boltasseva, H.A. Atwater, Low-loss plasmonic metamaterials, Science 331 (2011) 290−291.

[15] G.V. Naik, V.M. Shalaev, A. Boltasseva, Alternative plasmonic materials: Beyond gold and silver, Adv. Mater. 25 (2013) 3264−3294.

[16] B. Saha, A. Shakouri, T.D. Sands, Rocksalt nitride metal/semiconductor superlattices: A new class of articially structured materials, Appl. Phys. Rev. 5 (2018) 021101.

[17] R.S. Ningthoujam, N.S. Gajbhiye, Synthesis, electron transport properties of transition metal nitrides and applications, Prog. Mater. Sci. 70 (2015) 50−154.

[18] P. Patsalas, N. Kalfagiannis, S. Kassavetis, G. Abadias, D.V. Bellas, Ch Lekka, et al., Conductive nitrides: Growth principles, optical and electronic properties, and their perspectives in photonics and plasmonics, Mater. Sci. Eng. R-Rep. 123 (2018) 1−55.

[19] D. Jena, R. Page, J. Casamento, P. Dang, J. Singhai, Z. Zhang, et al., The new nitrides: Layered, ferroelectric, magnetic, metallic and superconducting nitrides to boost the GaN photonics and electronic eco-system, Jpn. J. Appl. Phys. 58 (2019) SC0801.

[20] C.-G. Ribbing, A. Roos, Transition-metal-nitride films for optical applications, Proc. SPIE 3133 (1997) 148−162.

[21] Z.-Y. Chiao, Y.-C. Chen, J.-W. Chen, Y.-C. Chu, J.-W. Yang, T.-Y. Peng, et al., Full-color generation enabled by refractory plasmonic crystals, Nanophotonics 11 (2022) 2891−2899.

[22] H. Wang, J. Li, K. Li, Y. Lin, J. Chen, L. Gao, et al., Transition metal nitrides for electrochemical energy applications, Chem. Soc. Rev. 50 (2021) 1354−1390.

[23] Y. Nakamura, H. Terai, K. Inomata, T. Yamamoto, W. Qiu, Z. Wang, Superconducting qubits consisting of epitaxially grown NbN/AlN/NbN Josephson junctions, Appl. Phys. Lett. 99 (2011) 212502.

[24] G.N. Gol'tsman, O. Okunev, G. Chulkova, A. Lipatov, A. Semenov, K. Smirnov, et al., Picosecond superconducting single-photon optical detector, Appl. Phys. Lett. 79 (2011) 705−707.

[25] P. Patsalas, S. Logothetidis, Optical, electronic, and transport properties of nanocrystalline titanium nitride thin films, J. Appl. Phys. 90 (2001) 4725−4734.

[26] M.B. Cortie, J. Giddings, A. Dowd, Optical properties and plasmon resonances of titanium nitride nanostructures, Nanotechnology 21 (2010) 115201.

[27] G.V. Naik, J. Kim, A. Boltasseva, Oxides and nitrides as alternative plasmonic materials in the optical range, Opt. Mater. Express 1 (2011) 1090−1099.

[28] G.V. Naik, J.L. Schroeder, X. Ni, A.V. Kildishev, T.D. Sands, A. Boltasseva, Titanium nitride as a plasmonic material for visible and near-infrared wavelengths, Opt. Mater. Express 2 (2012) 478−489.

[29] U. Guler, J.C. Ndukaife, G.V. Naik, A.G.A. Nnanna, A.V. Kildishev, V.M. Shalaev, et al., Local heating with lithographically fabricated plasmonic titanium nitride nano-particles, Nano Lett. 13 (2013) 6078−6083.

[30] A. Boltasseva, V.M. Shalaev, All that glitters need not be gold, Science 347 (2015) 1308−1310.

[31] B.T. Diroll, S. Saha, V.M. Shalaev, A. Boltasseva, R.D. Schaller, Broadband ultrafast dynamics of refractory metals: TiN and ZrN, Adv. Optical Mater. 8 (2020) 2000652.

[32] J.T. Hu, X.C. Ren, A.N. Reed, T. Reese, D. Rhee, B. Howe, et al., Evolutionary design and prototyping of single crystalline titanium nitride lattice optics, ACS Photonics 4 (2017) 606−612.

[33] T. Reese, A.N. Reed, A.D. Sample, F. Freire-Fernández, R.D. Schaller, A.M. Urbas, et al., Ultrafast spectroscopy of plasmonic titanium nitride nanoparticle lattices, ACS Photonics 8 (2021) 1556−1561.

[34] H. Wang, Q. Chen, L. Wen, S. Song S, X. Hu, G. Xu, Titanium-nitride-based integrated plasmonic absorber/emitter for solar thermophotovoltaic application, Photonics Res. 3 (2015) 329−334.

[35] M. Chirumamilla, A. Chirumamilla, Y. Yang, A.S. Roberts, P.K. Kristensen, K. Chaudhuri, et al., Large-area ultrabroadband absorber for solar thermophotovoltaics based on 3D titanium nitride nanopillars, Adv. Opt. Mater. 5 (2017) 1700552.

[36] D. Huo, J. Zhang, H. Wang, X. Ren, C. Wang, H. Su, et al., Broadband perfect absorber with monolayer MoS_2 and hexagonal titanium nitride nano-disk array, Nanoscale Res. Lett. 12 (2017) 465.

[37] Z.Y. Yang, S. Ishii, A.T. Doan, S.L. Shinde, T.D. Dao, Y.P. Lo, et al., Narrow-band thermal emitter with titanium nitride thin film demonstrating high temperature stability, Adv. Opt. Mater. 8 (2020) 1900982.

[38] M.-J. Yu, C.-L. Chang, H.-Y. Lan, Z.-Y. Chiao, Y.-C. Chen, H.W.H. Lee, et al., Plasmon-enhanced solar-driven hydrogen evolution using titanium nitride metasurface broadband absorbers, ACS Photonics 8 (2021) 3125−3132.

[39] W. He, K. Ai, C. Jiang, Y. Li, X. Song, L. Lu, Plasmonic titanium nitride nanoparticles for in vivo photoacoustic tomography imaging and photothermal cancer therapy, Biomaterials 132 (2017) 37−47.

[40] G. Qiu, S.P. Ng, C.-M.L. Wu, Label-free surface plasmon resonance biosensing with titanium nitride thin film, Biosens, Bioelectron. 106 (2018) (2018) 129−135.

[41] J. Gosciniak, F.B. Atar, B. Corbett, M. Rasras, CMOS-compatible titanium nitride for on-chip plasmonic Schottky photodetectors, ACS Omega 4 (2019) 17223−17229.

[42] M.R. Vissers, J. Gao, D.S. Wisbey, D.A. Hite, C.C. Tsuei, A.D. Corcoles, et al., Low loss superconducting titanium nitride coplanar waveguide resonators, Appl. Phys. Lett. 97 (2010) 232509.

[43] S. Ohya, B. Chiaro, A. Megrant, C. Neill, R. Barends, Y. Chen, et al., Room temperature deposition of sputtered TiN films for superconducting coplanar waveguide resonators, Supercond. Sci. Technol. 27 (2014) 15009.

[44] A. Shearrow, G. Koolstra, S.J. Whiteley, N. Earnest, P.S. Barry, F.J. Heremans, et al., Atomic layer deposition of titanium nitride for quantum circuits, Appl. Phys. Lett. 113 (2018) 212601.

[45] H.A. Smith, S. Elhamri, K.G. Eyink, L. Grazulis, M.J. Hill, T.C. Back, et al., Epitaxial titanium nitride on sapphire: Effects of substrate temperature on microstructure and optical properties, J. Vac. Sci. Technol. A 36 (2018) 03E107.

[46] E. Langereis, S.B.S. Heil, M.C.M. Van De Sanden, W.M.M. Kessels, In situ spectro-scopic ellipsometry study on the growth of ultrathin TiN films by plasma-assisted atomic layer deposition, J. Appl. Phys. 100 (2006) 023534.

[47] S. Murai, K. Fujita, Y. Daido, R. Yasuhara, R. Kamakura, K. Tanaka, Plasmonic arrays of titanium nitride nanoparticles fabricated from epitaxial thin films, Opt. Express 24 (2016) 1143.

[48] R.P. Sugavaneshwar, S. Ishii, T.D. Dao, A. Ohi, T. Nabatame, T. Nagao, Fabrication of highly metallic TiN films by pulsed laser deposition method for plasmonic appli-cations, ACS Photonics 5 (2018) 814−819.

[49] K.C. Maurya, V.M. Shalaev, A. Boltasseva, B. Saha, Reduced optical losses in refractory plasmonic titanium nitride thin films deposited with molecular beam epi-taxy, Opt. Mater. Express 10 (2020) 2679−2692.

[50] C.J.K. Richardson, A. Alexander, C.G. Weddle, B. Arey, M. Olszta, Low-loss super-conducting titanium nitride grown using plasma-assisted molecular beam epitaxy, J. Appl. Phys. 127 (2020) 235302.

[51] I.-H. Ho, C.-W. Chang, Y.-L. Chen, W.-Y. Chang, T.-J. Kuo, Y.-J. Lu, et al., Ultrathin TiN epitaxial films as transparent conductive electrodes, ACS Appl. Mater. Interfaces 14 (2022) 16839−16845.

[52] K. Minn, A. Anopchenko, Y.-J. Lu, C.-W. Chang, R. Mishra, J. Kim, et al., Enhanced spontaneous emission of monolayer MoS_2 on epitaxially grown titanium nitride epsilon-near-zero thin films, Nano Lett. 21 (2021) 4928−4936.

[53] R.A. Maniyara, D. Rodrigo, R. Yu, J. Canet-Ferrer, D.S. Ghosh, R. Yongsunthon, et al., Tunable plasmons in ultrathin metal films, Nat. Photon. 13 (2019) 328−333.

[54] Z.M. Abd El-Fattah, V. Mkhitaryan, J. Brede, L. Fernández, C. Li, Q. Guo, et al., Plasmonics in atomically thin crystalline silver films, ACS Nano 13 (2019) 7771−7779.

[55] A.R. Smith, K.-J. Chao, Q. Niu, C.-K. Shih, Formation of atomically flat silver films on GaAs with a "silver mean" quasi periodicity, Science 273 (1996) 226−228.

[56] R. Lemasters, C. Zhang, M. Manjare, W. Zhu, J. Song, S. Urazhdin, et al., Ultrathin wetting layer-free plasmonic gold films, ACS Photonics 6 (2019) 2600−2606.

[57] D.S. Katzer, N. Nepal, D.J. Meyer, B.P. Downey, V.D. Wheeler, D.F. Storm, et al., Epitaxial metallic β-Nb_2N films grown by MBE on hexagonal SiC substrates, Appl. Phys. Express 8 (2015) 085501.

[58] R. Yan, G. Khalsa, S. Vishwanath, Y. Han, J. Wright, S. Rouvimov, et al., GaN/NbN epitaxial semiconductor/superconductor heterostructures, Nature 555 (2018) 183−189.

[59] N.C. Saha, H.G. Tompkins, Titanium nitride oxidation chemistry: An X-ray photo-electron spectroscopy study, J. Appl. Phys. 72 (1992) 3072−3079.

[60] R. Zhang, Q.-Y. Ma, H. Liu, T.-Y. Sun, J. Bi, Y. Song, et al., Crystal orientation-dependent oxidation of epitaxial TiN films with tunable plasmonics, ACS Photonics 8 (2021) 847−856.

[61] D. Jaeger, J. Patscheider, Single crystalline oxygen-free titanium nitride by XPS, Surf. Sci. Spectra 20 (2013) 1−8.

[62] D. Shah, H. Reddy, N. Kinsey, V.M. Shalaev, A. Boltasseva, Optical properties of plasmonic ultrathin TiN films, Adv. Opt. Mater. 5 (2017) 1700065.

[63] D. Shah, A. Catellani, H. Reddy, N. Kinsey, V. Shalaev, A. Boltasseva, et al., Controlling the plasmonic properties of ultrathin TiN films at the atomic level, ACS Photonics 5 (2018) 2816−2824.

[64] A.S. Roberts, M. Chirumamilla, D. Wang, L. An, K. Pedersen, N.A. Mortensen, et al., Ultra-thin titanium nitride films for refractory spectral selectivity, Opt, Mater. Express 8 (2018) 3717−3728.

[65] M. Zahirul Alam, I. De Leon, R.W. Boyd, 742−760; Large optical nonlinearity of indium tin oxide in its epsilon-near-zero region, Science 352 (2016) 795−797.

[66] L. Braic, N. Vasilantonakis, A. Mihai, I.J. Villar Garcia, S. Fearn, B. Zou, et al., Titanium oxynitride thin films with tunable double epsilon-near-zero behavior for nanophotonic applications, ACS Appl. Mater. Interfaces 9 (2017) 29857−29862.

[67] N. Kinsey N, C. DeVault C, A. Boltasseva, V.M. Shalaev, Near-zero-index materials for photonics, Nat. Rev. Mater. 4 (2019) 742−760.

[68] M. Hövel, B. Gompf, M. Dressel, Dielectric properties of ultrathin metal films around the percolation threshold, Phys. Rev. B 81 (2010) 035402.

[69] H. Van Bui, A.Y. Kovalgin, J. Schmitz, R.A.M. Wolters, Conduction and electric field effect in ultra-thin TiN films, Appl. Phys. Lett. 103 (2013) 051904.

[70] W. Shockley, H.J. Queisser, Detailed balance limit of efficiency of p-n junction solar cells, J. Appl. Phys. 31 (1961) 510−519.

[71] R.M. Swanson, A proposed thermophotovoltaic solar energy conversion system, Proc. IEEE 67 (1979) 446−447.

[72] P.A. Davies, A. Luque, Solar thermophotovoltaics: Brief review and a new look, Sol. Energy Mater. Sol. Cell 33 (1994) 11−22.

[73] S. Fan, An alternative "Sun" for solar cells, Nat. Nanotechnol. 9 (2014) 92−93.

[74] N. Horiuchi, Efficient thermophotovoltaics, Nat. Photonics 14 (2020) 66.

[75] E. Rephaeli, S. Fan, Absorber and emitter for solar thermo-photovoltaic systems to achieve efficiency exceeding the Shockley-Queisser limit, Opt. Express 17 (2009) 15145−15159.

[76] N.-P. Harder, P. Würfel, Theoretical limits of thermophotovoltaic solar energy conversion, Semicond. Sci. Technol. 18 (2003) S151−S157.

[77] Y. Wang, H. Liu, J. Zhu, Solar thermophotovoltaics: Progress, challenges, and opportunities, APL. Mater. 7 (2019) 080906.

[78] A. Lenert, D.M. Bierman, Y. Nam, W.R. Chan, I. Celanović, M. Soljačić, et al., A nanophotonic solar thermophotovoltaic device, Nat. Nanotechnol, 9, 2014, pp. 126−130.

[79] M.W. Knight, H. Sobhani, P. Nordlander, N.J. Halas, Phtotodetection with active optical antennas, Science 332 (2011) 702−704.

[80] S. Linic, P. Christopher, D.B. Ingram, Plasmonic-metal nanostructures for efficient conversion of solar to chemical energy, Nat. Mater. 10 (2011) 911−921.

[81] K.R. White, K. Catchpole, Plasmon-enhanced internal photoemission for photovoltaics: Theoretical efficiency limits, Appl. Phys. Lett. 101 (2012) 073905.

[82] C. Clavero, Plasmon-induced hot-electron generation at manoparticle/metal-oxide interfaces for photovoltaic and photocatalytic devices, Nat. Photonics 8 (2014) 95−103.

[83] M.L. Brongersma, N.J. Halas, P. Nordlander, Plasmon-induced hot carrier science and technology, Nat. Nanotechnol. 10 (2015) 25−34.

[84] K. Song, H. Lee, M. Lee, J.Y. Park, Plasmonic hot hole-driven water splitting on Au nanoprisms/p-type GaN, ACS Energy Lett. 6 (2021) 1333−1339.

[85] G. Tagliabue, J.S. Duchene, A. Habib, R. Sundararaman, H.A. Atwater, Hot-hole *versus* hot-electron transport at Cu/GaN heterojunction interfaces, ACS Nano 14 (2020) 5788−5797.

[86] A. Moatti, J. Narayan, High-quality TiN/AlN thin film heterostructures on *c*-sapphire, Acta Materialia 145 (2018) 134−141.